Mechanical behavior of idealized, stingray-skeleton-inspired tiled composites as a function of geometry and material properties

AK Jayasankar[1], R Seidel[1], J Naumann[1], L Guiducci[1, 2], A Hosny[3], P Fratzl[1], JC Weaver[3], JWC Dunlop[1], MN Dean[1]

1. Max Planck Institute of Colloids and Interfaces, Germany
2. Cluster of Excellence, Humboldt-Universität zu Berlin
3. Wyss Institute at Harvard University, USA

Abstract

Tilings are constructs of repeated shapes covering a surface, common in both manmade and natural structures, but in particular are a defining characteristic of shark and ray skeletons. In these fishes, cartilaginous skeletal elements are wrapped in a surface tessellation, comprised of polygonal mineralized tiles linked by flexible joints, an arrangement believed to provide both stiffness and flexibility. The aim of this research is to use two-dimensional analytical models to evaluate the mechanical performance of stingray skeleton-inspired tessellations, as a function of their material and structural parameters. To calculate the effective modulus of modeled composites, we subdivided tiles and their surrounding joint material into simple shapes, for which mechanical properties (i.e. effective modulus) could be estimated using a modification of traditional Rule of Mixtures equations, that either assume uniform strain (Voigt) or uniform stress (Reuss) across a loaded composite material. The properties of joints (thickness, Young's modulus) and tiles (shape, area and Young's modulus) were then altered, and the effects of these tessellation parameters on the effective modulus of whole tessellations were observed. We show that for all examined tile shapes (triangle, square and hexagon) composite stiffness increased as the width of the joints was decreased and/or the stiffness of the tiles was increased; this supports hypotheses that the narrow joints and high tile to joint stiffness ratio in shark and ray cartilage optimize composite tissue stiffness. Our models also indicate that, for simple, uniaxial loading, square tessellations are least sensitive and hexagon tessellations most sensitive to changes in model parameters, indicating that hexagon tessellations are the most "tunable" to specific mechanical properties. Our models provide useful estimates for the tensile and compressive properties of 2d tiled composites under uniaxial loading. These results lay groundwork for future studies into more complex (e.g. biological) loading scenarios and three dimensional structural parameters of biological tilings, while also providing insight into the mechanical roles of tessellations in general and improving the design of bioinspired materials.

Keywords: Tessellations, Rule of mixtures, tiled composites, effective modulus, tessellated cartilage

1. Introduction

The tiling of surfaces with repeated geometric elements is a common structural motif in biological tissues and one that transcends phylogeny. Structural tilings have evolved independently in multiple systems and at a variety of size scales: from the micron-scale plates in the layers of nacre in mollusc shells (Barthelat and Zhu, 2011), to the sub-millimeter mineralized tiles (tesserae) sheathing the cartilages of sharks and rays (Seidel et al., 2016), to the macroscopic plates in the body armors of boxfish (Yang et al., 2015) and turtle shells (Chen et al., 2015; Krauss et al., 2009) as shown in Figure 1a. The mechanical characteristics of tiled natural composites are typically impressive amalgamations of those of their mineralized and organic component parts, resulting in natural armors that can be both lightweight and puncture resistant, but also flexible and tough (Chen et al., 2015; Krauss et al., 2009; Liu et al., 2010; Liu et al., 2014; Martini and Barthelat, 2016; Rudykh et al., 2015; Yang et al., 2013; Yang et al., 2012). The shapes and materials of the tiling subunits, their spatial arrangement, and their physical interactions control composite functional properties, guiding deformation and hindering damage propagation (Krauss et al., 2009; Liu et al., 2010; Vernerey and Barthelat, 2010; Yang et al., 2015). Analytical and experimental models of suture behavior, for instance, show that simple adjustments to the geometry and/or attachment areas of sutural teeth can be used to tune the mechanical properties (e.g. stiffness, strength, toughness), deformation or failure behaviors of a structured composite (Krauss et al., 2009; Li et al., 2013; Lin et al., 2014).

Figure 1: a. Examples of natural tilings, none of which are true tessellations due to overlapping (mollusc nacre) or interdigitating (turtle shell, boxfish scute) morphologies. b. Polygonal and square tessellations found in stingray cartilage. Organism and tissue images are compiled from a variety of species: a. Turbo caniculatus (mollusc shell), Haliotis rufescens (nacre); Phrynops geoffroanus (turtle shell); Ostracion rhinorhynchos (boxfish and scute inset; MCZ4454), Lactoria cornuta (interdigitations). b. Myliobatis freminvillei (stingray; USNM204770), Myliobatis californica (jaws; MCZ886), Aetobatus narinari (square tessellation), Leucoraja erinacea (polygonal tessellation).

The surface tiling of the skeleton of sharks and rays (elasmobranch fishes) has been recognized for over a century as a diagnostic character of all living members of this group, but the functional significance of this feature remains unclear. The tiled layer of elasmobranch cartilage, like most natural tilings, is comprised of hard inclusions/tiles (tesserae; Figure 1b) joined by unmineralized collagen fibers (Fig. 2c; see also Seidel et al., 2016). However, elasmobranch tesserae lack the interdigitations found in many other biological tilings, such as those seen in turtle osteoderms or boxfish scutes (Figure 1a) (Chen et al., 2015; Krauss et al., 2009; Yang et al., 2015). Furthermore, unlike the dermal scales of fishes, armadillo and some mammals, arrays of tesserae lack appreciable gaps or overlaps, and so can be considered “true tessellations” (Bruet et al., 2008; Chen et al., 2015; Wang et al., 2016; Yang et al., 2012). Elasmobranch tesserae also represent an intermediate size class of biological tiles, being typically hundreds of microns in size, an order of magnitude larger than mollusc nacre platelets and at least an order of magnitude smaller than most scales and osteoderms (Chen et al., 2015; Olson et al., 2012). The

tessellation of the elasmobranch skeleton is believed to manage stress distribution in a way that can minimize damage to the cartilage and also provide both flexibility and stiffness (Fratzl et al., 2016; Liu et al., 2010; Liu et al., 2014), the latter being somewhat counterintuitive considering the lack of obvious interlocking features between tesserae. The correlation between the structural and material aspects of tesserae and the mechanical properties of the skeleton at a larger scale remain undemonstrated. In particular, although elasmobranch tessellation is apparently largely comprised of hexagonal tiles (Dean and Schaefer, 2005; Dean et al., 2016; Seidel et al., 2016), other shapes are possible (Figure 1b); however, the role of tile shape in the mechanics of the tessellated composite (i.e. at the level of the skeletal tissue) has never been investigated.

In the current paper, our objectives are to analytically model biologically-inspired tessellated composites constructed with different tile types (triangle, square and hexagon) to observe the effects of (1) tile shape, (2) joint/tile size and (3) joint/tile material properties on the mechanical behavior (specifically, the effective stiffness) of the composite material (variables shown in Figure 2c). Our results establish a baseline for future analyses of tessellations with more complicated (e.g. biologically relevant) morphologies (e.g. ~~2.5 and~~ 3D tessellations) and loading conditions (e.g. bending, shear ~~, off-axis~~ and multi-axial loading). The results presented in this study improve our understandings of the functional significance of the tesseral morphologies observed in elasmobranch skeletons, while also framing form-function laws for engineered tiled composites.

2. Methods

2.1 Modified Rule of Mixtures model

To estimate the mechanical characteristics of our tessellated composites, we modify traditional Rule of Mixtures methods, which allow calculation of the contributions of constituent phases to the net stiffness of a composite. These methods permit the modeling of different materials arranged either in parallel (Voigt iso-strain model) or in series (Reuss iso-stress model), taking into account their volume fractions (VF) and stiffnesses (E1 and E2) (Bayuk et al., 2008). Geometrical interpretations of the Voigt and Reuss models are shown in Figure 2a.

Figure 2: a. Rule of Mixtures: Reuss and Voigt models. b. Orientation of model with respect to direction of load and the effect on joint material Young's modulus and composite effective modulus (modified Rule of Mixtures). *c. Structural and material properties of tessellations varied in this study, including shape, tile/joint material, and tile area/joint width. d. Modelling of the composite with the inspiration derived from Urobatis halleri (see text for explanation); the partition of hexagonal tile composite. See the Appendix for full derivations for all three tile shapes.*

The classical Rule of Mixtures models assume monolithic constituent materials with no anisotropy of material properties, arranged either in series with or perpendicular to loading orientation. This assumption is reasonable for calculating the effective modulus of a composite where materials are arranged in simple geometries and where loading orientation plays no role on a constituent material's properties.

The arrangement and morphology of joint material in tessellated cartilage, however, argue for a degree of orientation-dependent behavior. Intertesseral joints are comprised of linearly arrayed collagen fibers, oriented perpendicular to tesseral edges (Seidel et al., 2016) (Figure 2c; see discussion of tesseral ultrastructure below), and given also that our investigated tile models possess edges where joint and tile material are neither in perfect series nor parallel arrangements relative to load (e.g. Section 1 in Fig. 2c), we employ the two following modifications to the traditional Rule of Mixtures models.

In the first modification, to approximate the mechanical behavior of the intertesseral joint material of elasmobranch cartilage (for which no experimental data exist; see Section 2.3 below), we assume the material properties of the joint material to resemble those of other vertebrate fibrous materials. We assume the Young's modulus of the joint material perpendicular to the tesseral edge ($E2^{0^\circ}$, in line with the joint fiber directions) to be 1500 MPa (the tensile modulus of tendon; Shadwick, 1990), whereas we assume the modulus orthogonal to the direction of joint fibers ($E2^{90^\circ}$) to be only 50 MPa (the compressive modulus of periodontal ligament; Rees and Jacobsen, 1997). This modification is a matter of a simple substitution of $E2^{90^\circ}$ for $E2^{0^\circ}$ where Voigt (in-parallel) models are used in our calculations (Eq.1 below).

In the second modification, we account for situations where the tile and joint interface is oblique to the loading direction (i.e. neither a pure in-series/Reuss nor parallel/Voigt arrangement), such as can be seen in the equations for triangle and hexagon composites in the Appendix. This is accomplished by the following equation, which exploits the Pythagorean trigonometric identity, $\cos^2\theta + \sin^2\theta = 1$, to scale the relative contributions of Voigt and Reuss models according to the angle of rotation (θ) of the composite relative to loading direction:

$$E=\cos^2\theta * [\text{Reuss model}] + \sin^2\theta * [\text{Voigt model}]$$

$$= \cos^2\theta * \left[\frac{E1 * E2^{0^\circ}}{E1*(1\text{-}AF) + E2^{0^\circ}*(AF)}\right] + \sin^2\theta * [(E1 * AF + E2^{90^\circ} * (1\text{-}AF)] \quad (1)$$

The equation functions as a pure Reuss model with $E2^{0^\circ}$ joint modulus when in series with the load (θ = 0°: $\sin^2 0° = 0$, $\cos^2 90° = 1$; Fig. 2b, left image) and a Voigt model with joint modulus $E2^{90^\circ}$ when tissues phases are oriented in parallel with the load (θ = 90°: $\sin^2 90° = 1$, $\cos^2 90° = 0$; Fig. 2b, right image), with intermediate values of θ resulting in values of E that are proportional mixes of the pure models. This equation therefore accounts for the effects of both fiber orientation and oblique joint-tile interfaces (i.e. whole model orientation) relative to axial loads.

Our equation is more suited to our modeling goals than Krenchel's modified Rule of Mixtures model (Aspden, 1988; Krenchel, 1964), which modifies a Voigt model to formulate the effects of the orientation of stiff fibers within a softer matrix on a composite's stiffness:

$$E_{composite} = \cos^4(\theta) * E_{fiber} * AF + E_{matrix} * (1 - AF)$$

The limitation of Krenchel's model is that it assumes only the effect of fiber material orientation with respect to the Voigt model and so for our purposes could only capture the effects of changing joint fiber orientation in an in-parallel loading scenario.

2.2 Application to tessellation models

To apply these models to tessellations constructed from arrays of triangular, square and hexagonal tiles, we divide each composite unit cell (the tile and half of its surrounding joint material) into simple geometric shapes containing tile and joint material for which effective modulus can be calculated using Equation 1. The subdivisions of the hexagonal tile are shown as an example in Figure 2d. Although we focus on only one composite cell in our approach, this provides an estimate of the stiffness of a periodic array of tiles, similar to what would be generated in a Finite Element (FE) model employing periodic boundary conditions (PBC; see Section 2.5 below).

The effective modulus of each unit cell portion is then calculated using the modified Rule of Mixture equations provided above (Figure 2b), as a function of tile side length (L), tile modulus (E1), joint thickness (t) and joint modulus (ranging from $E2^{0^\circ}$ to $E2^{90^\circ}$, depending on the orientation to the loading direction). The effective modulus of the entire tile-joint composite (E) is then determined by combining the contributions of each of the unit cell portions, using traditional Voigt/Reuss models, according to their volume fractions relative to the whole and whether the subunits are arranged in parallel or series (e.g. Section 1 and 2 in Fig. 2d are arranged in series). The full calculations and assumptions of these models are provided in the Appendix. Using this approach, the effective modulus of the three tiled composites (comprised of triangle, square and hexagonal tiles) is evaluated. Alternate partitioning of unit cells (i.e. using other lines of division) had little effect on model results and only for the thickest joint morphologies for triangle and hexagon unit cells; this was a function of the different partitioning schemes altering whether the extreme corners of unit cell were assigned as oblique or in-series elements (data and partition schemes are provided in the Appendix).

The basic Voigt and Reuss models are shown in Figure 2a. When calculated using the same volume fractions of tile and joint materials as those in our composite models, these models act as upper and lower theoretical bounds, respectively, for our data. The mechanical behavior of the Voigt model (upper bound) is dictated by the properties of the stiffer material (tile = E1), given the assumption that the strains are uniform across the composite, due to the two phases of the composite being in parallel. In the Reuss model (lower bound), the properties are dominated by the softer material at 0° orientation to the load (joint = $E2^{0^\circ}$), due to the in-series orientation of the phases, resulting in uniform stresses across the composite.

2.3 Model constraints and biological relevance

In terms of inputs for our models, information on the structural and material properties of tessellated cartilage is limited, with the most information available on tesseral ultrastructure. Tesserae in curved regions of shark and ray skeletal elements may have more block-like, columnar or spherical morphologies (Dean et al., 2016; Fig. 1 in Liu et al., 2014; Fig. 2 in Seidel et al., 2016), but as their interactions with neighboring tesserae are more 3-dimensional, we derive the following synthesis of tesseral morphology from flat regions of the skeleton, where tesserae are more plate-like (e.g. Dean et al., 2016; see Fig. 10 in Seidel et al., 2016). Evidence from a variety of species indicates that tesserae can range from four- to twelve-sided, but are mostly hexagonal (Dean and Schaefer, 2005; Dean et al., 2016; Seidel et al., 2016) and that tesserae in adult animals are typically between ~200-500μm wide (within the plane of the tesseral mat), with little space between them (Clement,

1992; Dean et al., 2009; Kemp and Westrin, 1979; Seidel et al., 2016). The intertesseral joint space (the region of interaction between two adjacent tesserae) has a complex morphology, comprised of regions where neighboring tesserae are in direct contact (intertesseral contact zones: ~1-5μm wide; Fig. 2d) and wider gaps filled with linearly arrayed collagen fibers (intertesseral fibrous zones: ~20-30μm wide; Fig. 2d) (Seidel et al., 2016).

Material property data for tesserae remain scarce and inconsistent. The Young's modulus for intertesseral joint fibers is unexamined, but we will assume it to be similarly anisotropic to other vertebrate fibrous tissues (see Section 2.1 above). The Young's modulus for hydrated shark and ray mineralized tissue, derived from nanoindentation, has been reported to span a massive range from 79 to 4000 MPa (Ferrara et al., 2013; Wroe et al., 2008). The reason for this measurement variation is unknown, but is likely due largely to methodology (sample preparation, indenter size), and also perhaps interspecies differences in tesseral shape/properties. Recent data have also shown extensive local variation in mineral density within tesserae (Seidel et al., 2016). Correlated measurements of mineral density from quantitative backscatter electron imaging and material property data from nanoindentation argue that some sub-regions of tesserae may be up to an order of magnitude stiffer than the previously reported maximum (up to ~35GPa; R Seidel, pers. comm.). A tesseral Young's modulus in the higher range of reported values (e.g. > 1 GPa) is further supported by the comparable properties of other mineralized skeletal tissues (e.g. Carter and Hayes, 1977; Currey, 1988), the observations of extremely high mineral densities in tesserae (R. Seidel, pers. comm.; Seidel et al., 2016) and the direct relationship between mineral density and indentation modulus in calcified cartilage and bone (Gupta et al., 2005).

2.4 Visualization and evaluation of data

Our analytical models were evaluated for $E1/E2^{0^\circ}$ from 1.0 (equal tile and joint moduli) to 25.0 (tile modulus 25x that of joint modulus), and for $t/\sqrt{A}$, from 0.0 (no joints) to 0.10 (e.g. 10% of the square's side length). These values cover a biologically-relevant range of tesseral properties, from the softest to stiffest estimates of tesseral and fiber material properties and from the narrowest to widest measurements of intertesseral gaps and tesserae (Fig. 2c). For reference, we indicate with a red dot in Figures 3b and 4 our best approximation of the properties of the tesserae of round stingray (*Urobatis halleri*), as this species is the most studied in terms of ultrastructure and material properties (e.g. Dean et al., 2009; Dean et al., 2016; Seidel et al., 2016; Wroe et al., 2008).

We generated 2D contour plots for each unit cell shape using compound non-dimensional variables that take into account all elements of our effective moduli equations (Figure 3). In these plots, the x-axis is the ratio of the stiffness of the tile material relative to the joint material ($E1/E2^{0^\circ}$) and the y-axis is the ratio of the thickness of the joint relative to a linear measure of tile size ($t/\sqrt{A}$), with the "topography" (colored contours) of the graph representing the relative effective modulus (REM) of the composite (the stiffness of the composite relative to its joint stiffness, $E/E2^{0^\circ}$). Therefore, moving in the positive x-direction corresponds to increasingly stiffer tiles (or softer joints) and moving in the positive y-direction, a thickening of the joints relative to tile dimensions. These unitless ratios allow

comparison of the effects of both material properties (x-axis) and structural/shape parameters (y-axis) on composite mechanical performance (REM).

The first order parameter controlling mechanical properties of a composite is the volume fraction of the components (Hull and Clyne, 1996; Wang et al., 2011), or area fraction (AF) of joint and tile material, in the case of our 2D tilings. As we are interested in the role of shape and size of tiles with respect to a "biologically relevant" joint layer (i.e. one of a particular, measureable thickness) we chose to compare our predictions for fixed values of $t/\sqrt{A}$ rather than AF. For comparative purposes, however, we include in the Appendix our results (Fig. A.9) plotted with respect to area fraction. As expected the graphs plotted in terms of AF show little variation among the three unit shapes, underlining the lesser effect of unit cell shape compared with that of area fraction.

Our chosen y-axis size metric ($t/\sqrt{A}$) produced similar results to other descriptors of tile/joint geometry, such as ratios of joint thickness (t) to tile length (L) or perimeter (p) (data not shown). Given our interest in using a y-axis metric that contains a linear measure of joint thickness, we use $t/\sqrt{A}$ because, among possible tile/joint geometry metrics (e.g. t/p, t/L), it is most comparable to the area fraction (an important element of the Voigt/Reuss equations). Also, as effective modulus calculations for the three unit shapes are most similar when tile areas (rather than side lengths or perimeters) are normalized (data not shown), the results reported below according to $t/\sqrt{A}$ represent a more stringent series of comparisons.

2.5 Simulation and experimental verification of models

The three unit cell types can be partitioned in several different ways. To test for consistency between methods, we compare the results of two different partitioning schemes (see Appendix).

To verify the efficacy of our analytical models, Finite Element (FE) models representing the three tilings were generated in ABAQUS from models built in Rhino computer-aided-design (CAD) software with the Grasshopper plug-in. A 1% compressive strain and PBCs were applied and the models tested over a range of E1/E2 values for relatively thick joints ($t/\sqrt{A}$ = ~0.07). The resultant stress-strain curves were used to calculate the models' composite stiffness and those compared to the composite effective stiffnesses estimated by our analytical models using the same input parameters. A more detailed description of the methods can be found in the Appendix.

3. Results and discussion

FEA and analytical calculations showed general agreement in their estimates of composite model stiffness as a function of E1/E2 and a given $t/\sqrt{A}$ value (Supplemental Fig. A.10). This supports our conjecture that our analytical models of a single tile and its surrounding joint material can be used to approximate the behavior of a larger tiled array, in a manner similar to FE models employing periodic boundary conditions (see Appendix). Furthermore, our results were largely consistent, regardless of the unit cell partitioning scheme used (see Appendix, Figures A.7, and A.8).

All data calculated from the analytical models fall within the range of values depicted in the lower bound (Reuss) and upper bound (Voigt) contour plots for their unit cell shape; the upper and lower bound contour plots exhibited similar form and magnitude for all unit cell

shapes, therefore, we show only those plots for the square unit cell as an example in the first row of Figure 3. For the lower bound, close to the x-axis, contour lines showed positive slopes that gradually decreased and leveled off to roughly horizontal lines at higher x-axis values. Such regions of more horizontal contour orientation (i.e. at higher x-axis values) indicate a more geometry-sensitive/material-insensitive system, where changes in joint thickness (y-axis) have an effect on REM, but changes in joint/tile material properties (x-axis) have little effect. In contrast, a more vertical arrangement of contours, like those fanning out from the y-axis in the upper bound plot, signify a more geometry-insensitive/material-sensitive system, where material property (x-axis) changes are important, but there is little effect of changes in joint thickness (y-axis) on the REM of the composite.

In general, all models showed an increase of composite REM moving clockwise through the contour plot (i.e. towards thinner joints and stiffer tiles), however the relative widths of their contours became more evenly spaced from square to triangle to hexagon. The three unit cell shapes (triangle, square and hexagon) show a continuum in contour plot topography: starting with the square's stacked, asymptoting contours (which resemble those of the lower bound), and moving from triangle to hexagon, contour slopes steepen, resulting in the hexagon's contours being more similar in shape to those of the upper bound graph (Fig. 3A). This argues for the models, from square to triangle to hexagon, behaving increasingly as hybrid iso-stress/iso-strain composites and less as pure iso-stress models.

The variation in shape and spacing of contour lines among the three unit cell shapes is indicative of differences among models in the degree to which structural and material property changes affect composite performance. For example, the lateral spacing of the contour steps reflects the relationship between x-axis and REM values: if REM values increase more slowly than x-axis values —as in the upper half of the square tiled array graph (Fig. 3A), where contours are comparatively broad— changes in tile modulus have limited effect on the composite's REM (i.e. square is a more material-insensitive unit cell at large joint thicknesses). By contrast, when contour lines/REM values match x-axis values (i.e. contour lines are vertical and $E/E2^{0^\circ} = E1/E2^{0^\circ}$), changes in tile modulus have a direct and corresponding effect on the composite's REM. The more vertically oriented contours of the hexagon array graph therefore illustrate that the mechanical behavior of the hexagonal array is, on average, controlled to a larger degree by the composite's material properties.

In contrast, the vertical spacing of contour steps reflects the relationship between structural properties (i.e. joint thickness) and REM values. The tighter vertical spacing of contours on the lower right-hand side of all graphs illustrates that arrays become more sensitive to changes in joint morphology as tile and joint moduli diverge (i.e. at higher x-axis values). The square array's graph shows the tightest and most horizontal arrangement of contours in this region. This indicates that, in comparison with the other unit cells, and for a given high tile stiffness (i.e. high x-axis value), changes in joint morphology (vertical movements parallel to the y-axis) result in large changes in composite modulus (i.e. the composite is very geometry-sensitive). By contrast, hexagons (and to a lesser degree, triangles) are more influenced by both changes in geometry and material, a function of their contours' stable positive slopes. The narrowing of comparable graph contours (i.e. those representing the same z-value range) from square to triangle to hexagon also represents an increase in composite effective stiffness. Hexagons are therefore overall the most efficient shape in terms of the transfer of constituent material properties to composite modulus.

Figure 3: Relative Effective Modulus (REM) for all tile shapes, as a function of E1/E2 (x-axis) and t/√A (y-axis). The legend for terminology and scale for all graphs is shown in the upper left corner; with increasing x-axis values, tiles become stiffer relative to joints, with increasing y-axis values, joints are thicker relative to tile size. The lower and upper bounds for the square tile are shown in the upper right corner; upper/lower bound graphs for triangle and hexagon tiles were similar. A. Contour plots for all shapes (y-axis scale: 0.0-0.1). B. A zoomed in view of the contour plot from Figure 3A, to focus on more biologically relevant y-axis values (0.0 - 0.01). The biologically relevant x- and y-axis values —calculated from the structural and material properties of round stingray (U. halleri) tesserae— are marked by a red marker. Note that whereas hexagon result in the stiffest composite behavior overall (i.e. the REM values are highest for any given x-value), all tile shapes have similar contour patterns for the biologically-relevant range in B indicating little effect of unit cell shape on REM for thin joints (low y-axis values).

The maximum y-axis value in Figure 3A represents comparatively thick joints (e.g. up to 10% of the square tile's side length), whereas those of the natural tessellated cartilage system are quite narrow (~1/500 width of the tile ~0.002L; Seidel et al., 2016). The contour plots in Figure 3B present a more biologically relevant y-axis scale, from 0 to 0.01, indicated by the horizontal white bars in 3a; x- and y-values representing stingray (*U. halleri*) cartilage are marked with red dots in Figs. 3B and 4. In Figure 3B, all tile shapes exhibit a fanned series of nearly vertical lines that, with increasing x-axis values, gradually tilted away from the y-axis. These nearly vertical contours signify that, when joints are thin, all models are more geometry-insensitive/material-sensitive systems, where material property (x-axis) changes are important, but there is little effect of changes in joint thickness (y-axis) on the REM of the composite. For very thin joints (i.e. Fig. 3B), the triangle model is slightly softer than the square model, a function of the shallower curves of its contours.

Figure 4: Comparison of the contour plots of all tile shapes from Figure 3. Contour lines originating from the same x-axis value (a contour line trio) correspond to the same z-axis value range (e.g. all lines in the first trio on the far left of 4A indicate REM = 2.5). The spread of contour line in a trio reflects the dissimilarity of the topography of the contour plots of the three tile shapes: in particular for the upper right portion of A, where joints are very thick and tiles are far stiffer than joints, the REM for hexagon is considerably higher than that of square. The narrower spread of contour lines in trios in biologically relevant range (B) indicates that unit cells exhibit more similar mechanical behavior at small y-axis values (e.g. narrow joints). A. Contour lines for all shapes (y-axis scale: 0.0-0.1); compare with Figure 3A. B. A zoomed in view of the contour plot lines from Figure 4A, to focus on more biologically relevant y-axis values (0.0 - 0.01); compare with Figure 3B. Values for the structural and material properties of round stingray (U. halleri) tesserae are marked by a black marker.

The degree of "geometry insensitivity" varies to some degree by shape: moving from triangle to square to hexagon the contours gradually incline more towards the left, indicating decreased susceptibility to changes in joint thickness (Fig. 4). For values of joint morphology measured from stingrays, however, these effects are minimal: from triangle to square to hexagon, the REM values only increase 1.45% of their x-axis (i.e. tile stiffness)

values, from 90.77% to 91.45% to 92.22%. This is further illustrated in Figure 5 in a two-dimensional graph of REM values for the biologically relevant morphologies ($t/\sqrt{A} = 0.002$). Overall, the similarity of the observed trends and the convergence of comparable contour lines near the x-axis of Figure 4 indicate that the thinner an array's joints, the less of a role tile shape plays in composite stiffness.

Figure 5: Two-dimensional graphical representation of REM for all tile shapes when t/sqrt(A)= 0.002 (biologically relevant value, derived from U. halleri tessellated cartilage), showing the relationship between tile and composite modulus. The zoomed in pane shows the high correspondence of the three unit cells' lines, indicating similar mechanical behavior at small y-axis values (e.g. narrow joints). All shapes fall within their respective upper and lower bounds; note that the upper bound lines are nearly overlapping and the lower bound for hexagon is hidden beneath the REM line for the triangle array. The region above the upper bound lines represents an unrealistic scenario where the composite is stiffer than its stiffest constituent (E>E1).

4. Conclusions

All examined models show stiffening of the composite when joint widths are minimized and/or tile stiffness is maximized. On average, however, the effective modulus of the square array is least sensitive and that of the hexagon array most sensitive to changes in model parameters. This suggests that square arrays would be less sensitive to structural/material variation (e.g. a wide range of $E1/E2^{0^\circ}$ values results in the same effective modulus, particularly when joints are thick), whereas hexagon tiled arrays would be more "tunable". Square tiled arrays also allow the least return on material investment in terms of stiffness, whereas hexagon arrays provide a more optimized solution by maximizing the contribution of the harder tile material to the stiffness of the whole composite, being at a minimum 70.8% as stiff as their stiffest material for the range of values investigated here (as compared with 66.7% for the square unit cell). These differences are even more pronounced when other variables of tile shape are held constant (e.g. tile length or perimeter, rather than area; data not shown), but global trends among unit cell shapes are consistent, with hexagons always out-performing the other shapes in terms of composite stiffness. In models of geometric sutural interfaces, where joint thickness and volume fraction were held constant, stiffness increased as the length of sutural tooth edges in contact with joint material was increased, via addition of extra joint material to bond tooth tips to their corresponding troughs or via increases in tooth tip angle for teeth with bonded tips (Lin et al., 2014). In contrast, in our models, for a given thickness of joint, hexagons —the tile that minimizes perimeter length for a given tile area— maximized composite model stiffness, by minimizing joint attachment surface and therefore the overall amount of joint material in the tiled composite. These observations on the mechanical efficiency of tiled composites are relevant to the laws constraining structuring of tiled biological materials, but also to manufacturing perspectives, where specific composite mechanical properties are desired.

The variable behaviors observed for different tile shapes when joints are thick do not apply for thin-jointed tile arrays, which converge on similar mechanical behaviors for the uniaxial loading regime simulated here. However, based on data showing the mechanical anisotropy of cellular solids (Ashby et al., 1995) and co-continuous composites (Wang et

al., 2011), and given the large angle between the sides of square tiles, we would expect that square arrays would be particularly sensitive to variations in loading direction and, in biological systems, would only be found in areas with restricted loading orientation. This is supported by our observation of square tesserae in specific areas of the jaws of myliobatid stingrays (Dean, pers. obs.; Figure 1b), directly beneath the tooth plates used to crush hard shelled prey with high, uniaxial bite forces (Kolmann et al., 2015; Summers, 2000).

Square tesserae are, however, otherwise apparently not common in tessellated cartilage, with limited data on shark and ray cartilage tessellations suggesting that hexagons are the most common tiling elements (Dean and Schaefer, 2005; Dean et al., 2016). Our data show that hexagonal tiles can, under some loading conditions, impart superior mechanical properties to composites, in comparison with square and triangle arrays. The effect of tile shape may be largely irrelevant in the biological system, however, considering that a recent survey of the tessellations of several shark and ray species suggested that intertesseral joints may, as a rule, be extremely narrow (Seidel et al., 2016). The predominance of hexagonal tiles could also relate to factors besides mechanics, such as biological growth mechanisms. For instance, given that tesserae arise from seed mineralization centers and grow by mineral accretion at their margins (Dean et al., 2009; Seidel et al., 2016), tesseral shape could also be regulated by the initial packing of mineralization seeds and/or variation in the local rates and uniformity of mineral deposition as tesserae and skeletal elements increase in size. In the latter case, tesserae with more sides could represent more uniform radial growth, whereas square tesserae would suggest a simpler biaxial growth pattern.

Our models provide theoretical groundwork for planned Finite Element simulations of more complex 3D tessellation models, but are currently only valid for in-plane, unidirectional loading (tension or compression), along the primary “vertical” axes of our unit cell shapes and for small resultant strains (see Appendix). Our results therefore give only an estimation of the tensile/compressive properties of tiled composites under instantaneous loading without, for example, capturing non-linear effects of tile-tile contact on mechanics, which may play a fundamental role in the mechanics of tessellated cartilage (Fratzl et al., 2016) and should also be very geometry dependent (Li et al., 2013). Our future studies will incorporate more detailed investigation through FE simulations and mechanical testing of 3D printed models, as well as the effects of off-axis loading, including shear and Poisson’s ratio effects, to better approximate the features of the biological tilings under study and provide insight into tiled composite architectures in general.

Acknowledgments

We would like to thank the organizers of the ‘*Articulated Structures and Dermal Armor*’ symposium at the 2015 International Conference on Mechanics of Biomaterials and Tissues for the opportunity to publish in this volume. We also thank Callie Crawford, Andrew Gillis, Matt Kolmann, James Michaelson in collaboration with the Virtual Museum of Natural History, Michael Porter, Tristan Stayton and Adam Summers for providing the scan data for the images in Figure 1. We also thank Bas Overvelde for his assistance in implementing his PBC code for our FE models. This work was supported by an HFSP Young Investigators’ Grant to MND and JCW (RGY0067-2013), a SYNTHESYS grant to MND (GB-TAF-2289), and a DFG-FR 2190/4-1 Gottfried Wilhelm Leibniz-Preis 2010.

References

Ashby, M., Gibson, L., Wegst, U., Olive, R., 1995. The mechanical properties of natural materials. I. Material property charts. Proceedings of the Royal Society of London A: Mathematical, Physical and Engineering Sciences 450, 123-140.

Aspden, R.M., 1988. The theory of fiber-reinforced composite-materials applied to changes in the mechanical-properties of the cervix during pregnancy. J Theor Biol 130, 213-221.

Barthelat, F., Zhu, D., 2011. A novel biomimetic material duplicating the structure and mechanics of natural nacre. Journal of Materials Research 26, 1203-1215.

Bayuk, I.O., Gay, J.K., Hooper, J.M., Chesnokov, E.M., 2008. Upper and lower stiffness bounds for porous anisotropic rocks. Geophysical Journal International 175, 1309-1320.

Bruet, B.J., Song, J., Boyce, M.C., Ortiz, C., 2008. Materials design principles of ancient fish armour. Nature Materials 7, 748-756.

Carter, D.R., Hayes, W.C., 1977. The compressive behavior of bone as a two-phase porous structure. The Journal of Bone & Joint Surgery 59, 954-962.

Chen, I.H., Yang, W., Meyers, M.A., 2015. Leatherback sea turtle shell: A tough and flexible biological design. Acta Biomaterialia 28, 2-12.

Clement, J.G., 1992. Re-examination of the fine structure of endoskeletal mineralization in Chondrichthyes: Implications for growth, ageing and calcium homeostasis. Australian Journal of Marine and Freshwater Research 43, 157-181.

Currey, J.D., 1988. The effect of porosity and mineral content on the Young's modulus of elasticity of compact bone. Journal of Biomechanics 21, 131-139.

Dean, M., Schaefer, J., 2005. Patterns of growth and mineralization in elasmobranch cartilage. FASEB Journal 19, A247-A247.

Dean, M.N., Mull, C.G., Gorb, S.N., Summers, A.P., 2009. Ontogeny of the tessellated skeleton: insight from the skeletal growth of the round stingray *Urobatis halleri*. Journal of Anatomy 215, 227-239.

Dean, M.N., Seidel, R., Knoetel, D., Lyons, K., Baum, D., Weaver, J., Fratzl, P., 2016. To build a shark-3D tiling laws of tessellated cartilage. 56, E50–E50.

Ferrara, T.L., Boughton, P., Slavich, E., Wroe, S., 2013. A novel method for single sample multi-axial nanoindentation of hydrated heterogeneous tissues based on testing great white shark jaws. PLoS ONE 8, e81196.

Fratzl, P., Kolednik, O., Fischer, F.D., Dean, M.N., 2016. The mechanics of tessellations–bioinspired strategies for fracture resistance. Chemical Society Reviews 45, 252-267.

Gupta, H., Schratter, S., Tesch, W., Roschger, P., Berzlanovich, A., Schoeberl, T., Klaushofer, K., Fratzl, P., 2005. Two different correlations between nanoindentation modulus and mineral content in the bone–cartilage interface. Journal of Structural Biology 149, 138-148.

Hull, D., Clyne, T.W., 1996. An introduction to composite materials, 2nd ed. Cambridge University Press, Cambridge ; New York.

Kemp, N.E., Westrin, S.K., 1979. Ultrastructure of calcified cartilage in the endoskeletal tesserae of sharks. Journal of Morphology 160, 75-101.

Kolmann, M.A., Huber, D.R., Motta, P.J., Grubbs, R.D., 2015. Feeding biomechanics of the cownose ray, *Rhinoptera bonasus*, over ontogeny. Journal of Anatomy 227, 341-351.

Krauss, S., Monsonego- Ornan, E., Zelzer, E., Fratzl, P., Shahar, R., 2009. Mechanical function of a complex three- dimensional suture joining the bony elements in the shell of the red- eared slider turtle. Adv Mater 21, 407-412.

Krenchel, H., 1964. Fibre Reinforcement: Theoretical and Practical Investigations of the Elasticity and Strength of Fibre-reinforced Materials. Akademisk Forlag, Copenhagen.

Li, Y., Ortiz, C., Boyce, M.C., 2013. A generalized mechanical model for suture interfaces of arbitrary geometry. J Mech Phys Solids 61, 1144-1167.

Lin, E., Li, Y., Ortiz, C., Boyce, M.C., 2014. 3D printed, bio-inspired prototypes and analytical models for structured suture interfaces with geometrically-tuned deformation and failure behavior. J Mech Phys Solids 73, 166-182.

Liu, X., Dean, M.N., Summers, A.P., Earthman, J.C., 2010. Composite model of the shark's skeleton in bending: A novel architecture for biomimetic design of functional compression bias. Materials Science and Engineering: C 30, 1077-1084.

Liu, X., Dean, M.N., Youssefpour, H., Summers, A.P., Earthman, J.C., 2014. Stress relaxation behavior of tessellated cartilage from the jaws of blue sharks. Journal of the Mechanical Behavior of Biomedical Materials 29, 68-80.

Martini, R., Barthelat, F., 2016. Stability of hard plates on soft substrates and application to the design of bioinspired segmented armor. J Mech Phys Solids 92, 195-209.

Olson, I.C., Kozdon, R., Valley, J.W., Gilbert, P.U.P.A., 2012. Mollusk shell nacre ultrastructure correlates with environmental temperature and pressure. Journal of the American Chemical Society 134, 7351-7358.

Overvelde, J.T.B., Bertoldi, K., 2014. Relating pore shape to the non-linear response of periodic elastomeric structures. J Mech Phys Solids 64, 351-366.

Rees, J., Jacobsen, P., 1997. Elastic modulus of the periodontal ligament. Biomaterials 18, 995-999.

Rudykh, S., Ortiz, C., Boyce, M.C., 2015. Flexibility and protection by design: imbricated hybrid microstructures of bio-inspired armor. Soft matter 11, 2547-2554.

Seidel, R., Lyons, K., Blumer, M., Zaslansky, P., Fratzl, P., Weaver, J.C., Dean, M.N., 2016. Ultrastructural and developmental features of the tessellated endoskeleton of elasmobranchs (sharks and rays). Journal of Anatomy 229, 681-702.

Summers, A.P., 2000. Stiffening the stingray skeleton-an investigation of durophagy in myliobatid stingrays (Chondrichthyes, Batoidea, Myliobatidae). Journal of Morphology 243, 113-126.

Vernerey, F.J., Barthelat, F., 2010. On the mechanics of fishscale structures. International Journal of Solids and Structures 47, 2268-2275.

Wang, B., Yang, W., Sherman, V.R., Meyers, M.A., 2016. Pangolin armor: Overlapping, structure, and mechanical properties of the keratinous scales. Acta Biomaterialia 41, 60-74.

Wang, L.F., Lau, J., Thomas, E.L., Boyce, M.C., 2011. Co-continuous composite materials for stiffness, strength, and energy dissipation. Adv Mater 23, 1524-1529.

Wroe, S., Huber, D.R., Lowry, M., McHenry, C., Moreno, K., Clausen, P., Ferrara, T.L., Cunningham, E., Dean, M.N., Summers, A.P., 2008. Three-dimensional computer analysis of white shark jaw mechanics: how hard can a great white bite? Journal of Zoology 276, 336-342.

Yang, W., Chen, I.H., Gludovatz, B., Zimmermann, E.A., Ritchie, R.O., Meyers, M.A., 2013. Natural flexible dermal armor. Advances Materials 25, 31-48.

Yang, W., Chen, I.H., McKittrick, J., Meyers, M.A., 2012. Flexible dermal armor in nature. JOM 64, 475-485.

Yang, W., Naleway, S.E., Porter, M.M., Meyers, M.A., McKittrick, J., 2015. The armored carapace of the boxfish. Acta Biomaterialia 23, 1-10.

Appendix

We apply modified Rule of Mixtures models to tessellations constructed from arrays of triangular, square and hexagonal tiles, by dividing each composite unit cell (the tile and its surrounding joint material) into simple geometric shapes containing tile and joint material. The justifications for these models are discussed in the Methods; we describe and illustrate the partitioning of each unit cell shape below.

Structure	MPa
E1 = Tile Young's modulus	35000 MPa
Young's modulus of joint of joint fibers at 0° orientation (i.e. in line with load) = $E2^{0°}$	1500 MPa
Young's modulus of joint at 90° orientation (i.e. perpendicular to load) = $E2^{90°}$	50 MPa

Table 1: Material properties of tile and joint materials.

Triangle

Figure A.1: Dimensions of triangle composite.

Length of the tile = L

Thickness of the joint = t

Length of the composite = L+2*h1

$h1 = \frac{t}{\tan 30°}$

Area of the composite = $\frac{\sqrt{3}}{4}$*(L+2h1)^2

Area of the tile = $\frac{\sqrt{3}}{4}$*(L)^2

Orientation of the fiber material relative to load = θ

Partitions

Figure A.2: Partitions in triangle composite.

Section 1 is marked with red lines whereas Section 2 is marked with a green line. Section 1L and Section 1R are mirror images of each other, therefore it is enough to solve the effective modulus of just Section 1L, which will have the same effective modulus as Section 1R and as the complete Section 1 (combination of Section 1L and Section 1R).

Computing the effective modulus of Section 1L ($E_{section1L}$)

Area of tile region in Section 1L $= \frac{1}{2} * \frac{\sqrt{3}}{4} * (L)^2$

Joint region in the Section 1L is trapezoid.

Area of joint region marked in red in Section 1L $= \frac{(L+L+2*h1)}{2} * t$

Total Area of Section 1L $= TA_1$

$$TA_1 = \frac{1}{2} * \frac{\sqrt{3}}{4} * (L)^2 + \frac{(L+L+2*h1)}{2} * t$$

Area fraction of tile region in Section 1L $= AF_1$

$$AF_{section1L} = \frac{\frac{1}{2} * \frac{\sqrt{3}}{4} * (L)^2}{\frac{1}{2} * \frac{\sqrt{3}}{4} * (L)^2 + \frac{(L+L+2*h1)}{2} * t}$$

$$E_{section1L} = \cos^2\theta * \frac{E1 * E2^{0°}}{E1*(1-AF_{section1L}) + E2^{0°} * (AF_{section1L})} + \sin^2\theta * (E1*AF_{section1L} + E2^{90°} * (1-AF_{section1L}))$$

Computing the effective modulus of composite ($E_{composite}$)

Total area of composite $= TA_{composite}$

$$TA_{composite} = \frac{\sqrt{3}}{4} * [\, L + 2\left(\frac{t}{\tan 30°}\right)\,]^2$$

Total area of Section 1 (L and R combined) $= \frac{\sqrt{3}}{4} * (L)^2 + 2 * (\frac{(L+L+2*h1)}{2} * t)$

Area fraction of the composite $= AF = \frac{\text{Total area of Section 1 and 2}}{TA_{composite}}$

$$AF = \frac{\frac{\sqrt{3}}{4} * (L)^2 + 2 * (\frac{(L+L+2*h1)}{2} * t)}{\frac{\sqrt{3}}{4} * [\, L + 2\left(\frac{t}{\tan 30°}\right)\,]^2}$$

$$E_{composite} = \frac{E_{section1} * E2^{0°}}{E_{section1} * (1 - AF_{section1\&2}) + E2^{0°} * AF_{section1\&2}}$$

Square

Figure A.3: Dimensions and partitions of square composite.

Length of the tile = L

Joint thickness = t

Length of the composite = L+2*t

Area of the composite $=(L+2*t)^2$

Area of the tile $= (L)^2$

Calculation the effective modulus for Section 1

Figure A.4: Dimensions and partitions of Section 2 in square composite.

Area of Section 1 =(L+2*t)*L

Area fraction of the Section 1 $(AF_1) = \frac{\text{Area of the tile}}{\text{Area of composite}}$

$$AF_{section1} = \frac{L^2}{L*(L+2*t)}$$

Effective modulus of Section 1= $E_{section1}$

$$E_{section1} = E_1 * AF_1 + E2^{90^\circ} * (1 - AF_1)$$

Computing the net effective modulus of the composite

$$\text{Area fraction (AF)} = \frac{\text{Total area of Section 1}}{\text{Total area of composite}} = \frac{L*(L+2*t)}{(L+2*t)^2} = \frac{L}{L + 2 * t}$$

Since Section 1 and Section 2 are in series and since both Section 2 elements (top and bottom joints) are composed only of joint material at 0° orientation, the net effective modulus of the square composite is:

$$E_{composite} = \frac{E_{section1} * E2^{0^\circ}}{E_{section1} * (1\text{-}AF) + E2^{0^\circ} * (AF)}$$

Hexagon

Figure A.5: Dimensions of hexagonal composite.

Length of the tile = L

Joint thickness = t

Length of the composite = L+a

$$a = \frac{t}{\sin 60°}$$

Area of the composite = $\frac{3\sqrt{3}}{2}*(L+a)^2$

Area of tile = $\frac{3\sqrt{3}}{2}*(L)^2$

θ = Orientation of the fiber material relative to load

Partitions

Figure A.6: Dimensions of partitions of hexagonal composite.

Section 1 is marked with red lines, whereas Section 2 is marked with a green line. Similar to triangle, Section 1 appears several times in the unit cell in mirrored, identical parts. It is enough to solve the effective modulus of the single Section 1 element shown in Figure A.6, which equals the effective modulus of all three additional Section 1 elements.

Effective modulus of Section 1:

Area of the tile in Section 1 = $\frac{1}{4} * \frac{3\sqrt{3}}{2}*(L)^2$

Area of the joint in Section 1 = $\frac{(2*L+a)}{2}*t$

$$AF_{section1} = \frac{\text{(Area of tile in Section 1)}}{\text{Area of tile in Section 1 + Area of joint in Section 1}} = \frac{(\frac{1}{4}*\frac{3\sqrt{3}}{2}*(L)^2)}{(\frac{1}{4}*\frac{3\sqrt{3}}{2}*(L)^2 + \frac{(2*L+a)}{2}*t)}$$

The effective modulus of the Section 1 is calculated below:

$$E_{section1} = \cos^2\theta * \frac{E1 * E2^{0°}}{E1*(1-AF_{section1}) + E2^{0°}*(AF_{section1})} + \sin^2\theta * (E1*AF_{section1} + E2^{90°}*(1-AF_{section1}))$$

Calculating area fraction of Section 2:

Area of the joint in Section 2 = $\frac{(2*L+a)}{2}*t$

Total area of all four Section 1 elements $= (\frac{3\sqrt{3}}{2} * (L)^2 + 4 * \frac{(L+L+a)}{2} * t)$

Area fraction of the composite $= AF = \frac{\text{Total area of Section 1}}{\text{Total area of composite}} = \frac{(\frac{3\sqrt{3}}{2} * (L)^2 + 4 * \frac{(2*L+a)}{2} * t)}{\frac{3\sqrt{3}}{2} * (L+a)^2}$

Effective modulus of the composite

$$E_{composite} = \frac{E_{section1} * E2^{0^\circ}}{E_{section1} * (1\text{-}AF) + E2^{0^\circ} * (AF)}$$

Alternative partition schemes:

The three unit cell types can be partitioned in several different ways. We present two schemes below, Schemes A and B and compare their results in Figure A.8. We consider Scheme A to be the more intuitive and so use it to generate our datasets.

Figure A.7: Partitioning schemes. Regions colored in red indicate corner elements that are assigned different properties as a function of the different partitioning schemes.

Comparison of results between partition schemes

Figure A.8: Comparison of contour lines scheme.

The effective modulus calculations for Schemes A and B are compared with each other by overlaying the contour lines of both the schemes over one another (Figure A.8 above). The further apart two comparable contour lines are (i.e. when both blue and red lines are visible), the more different the results generated by the schemes. It is evident that there is no difference in the REM for both the partitioning schemes for biologically relevant values (lower graphs, marked in red). Differences are most pronounced for very thick joints for hexagon and triangle tiles; this is due to the corner regions in the oblique elements (e.g. Section 1 of triangle and hexagon), marked in red in Figure A.7, which can be considered either as pure in-series elements (Reuss) or off-axis elements (hybrid Reuss-Voigt; see 2. Methods).

Effect of area fraction on relative effective modulus of all shapes

Figure A.9: Comparison of relative effective modulus for all shapes with respect to area fraction reflecting the REM values for all shapes lie in same contour region.

Verification and Experimental methods

The verification procedure for the derived analytical equations was performed using finite element analysis (FEA). The tiling network is modeled in the CAD software Rhino, using the Grasshopper plugin for parameterized modelling. Since the structure of the tiling network is complex (e.g. the joints are very thin compared tiles and would require a fine meshing to capture their performance), modeling a large tiled network would demand considerable computational power and time. We overcame this by using Periodic Boundary Conditions (PBC) (Li et al., 2013; Overvelde and Bertoldi, 2014), sets of equations to model large systems by breaking them into small parts (representative volume elements RVE; Fig. x) that can be repeated periodically over the space to approximate the larger network. Since RVEs are identical in terms of structural and material properties, their responses to the acting forces are the same.

Figure A.10: Comparison of relative effective modulus (E/E2) between analytical calculations, FEA(periodic boundary conditions) and FEA(tiled array) with E1/E2 on x-axis and E/E2 on y-axis.

In our models, a 2-dimensional RVE (with biologically relevant morphology, $t/\sqrt{A} = 0.002$) was modeled for hexagon, square and triangle tilings using Rhino and Grasshopper. RVEs were imported into ABAQUS (FEA) software and simulations performed for simple compression (1% strain) of the models, with PBCs applied via a readily available PYTHON code (Overvelde and Bertoldi, 2014). Models were tested over a range of E1/E2 values (Fig. A.10), from E1/E2 = 5.0 to 23.3, the biologically relevant tile to joint material stiffness ratio. Each composite model's stiffness was measured as the ratio between the average stress (Total Reaction Force on the boundary / RVE side length) and the average strain (the 1% imposed to the RVE). A uniform joint material property ($E2^{0^\circ} = 1500$ MPa) was used (i.e. with loading orientation having no effect on joint modulus), as orientation-dependent material properties are beyond the scope of the current paper. Furthermore, since the joints are very thin in the biologically relevant morphology (i.e. the joint area fraction is low), the differences with the analytical models, where the effect of joint orientation is considered, should be negligible.

Summary

<table>
<tr><th>Triangle</th><th>Square</th><th>Hexagon</th></tr>
<tr><td>Area of the composite
$\frac{\sqrt{3}}{4}*(L+2*\frac{t}{0.57})^2$</td><td>Area of the composite
$(L+2*t)^2$</td><td>Area of the composite
$\frac{3\sqrt{3}}{2}*(L+\frac{t}{0.86})^2$</td></tr>
<tr><td>Area of the tile
$\frac{\sqrt{3}}{4}*L^2$</td><td>Area of the tile
L^2</td><td>Area of the tile
$=\frac{3\sqrt{3}}{2}*L^2$</td></tr>
<tr><td>Area of the joint
$3*(2*L+\frac{t}{0.57})*t/2$</td><td>Area of the joint
$(L+2*t)^2- L^2$</td><td>Area of the joint
$3*t*(2*L+\frac{t}{0.86})$</td></tr>
<tr><td>Perimeter
<table><tr><td>Tile</td><td>$3*L$</td></tr><tr><td>Composite</td><td>$3*(L+2*\frac{t}{0.57})$</td></tr></table></td><td>Perimeter
<table><tr><td>Tile</td><td>$4*L$</td></tr><tr><td>Composite</td><td>$4*(L+2*t)$</td></tr></table></td><td>Perimeter
<table><tr><td>Tile</td><td>$6*L$</td></tr><tr><td>Composite</td><td>$6*(L+\frac{t}{0.86})$</td></tr></table></td></tr>
<tr><td>Area fraction:
Area of tile/Area of composite
$\frac{(L)^2}{(L+2*\frac{t}{0.57})^2}$</td><td>Area fraction:
Area of tile/Area of composite
$\frac{(L)^2}{(L+2*t)^2}$</td><td>Area fraction:
Area of tile/Area of composite
$\frac{(L)^2}{(L+\frac{t}{0.86})^2}$</td></tr>
</table>

Table A.1: Summary of structural parameters and their formulae for all shapes.

Figures

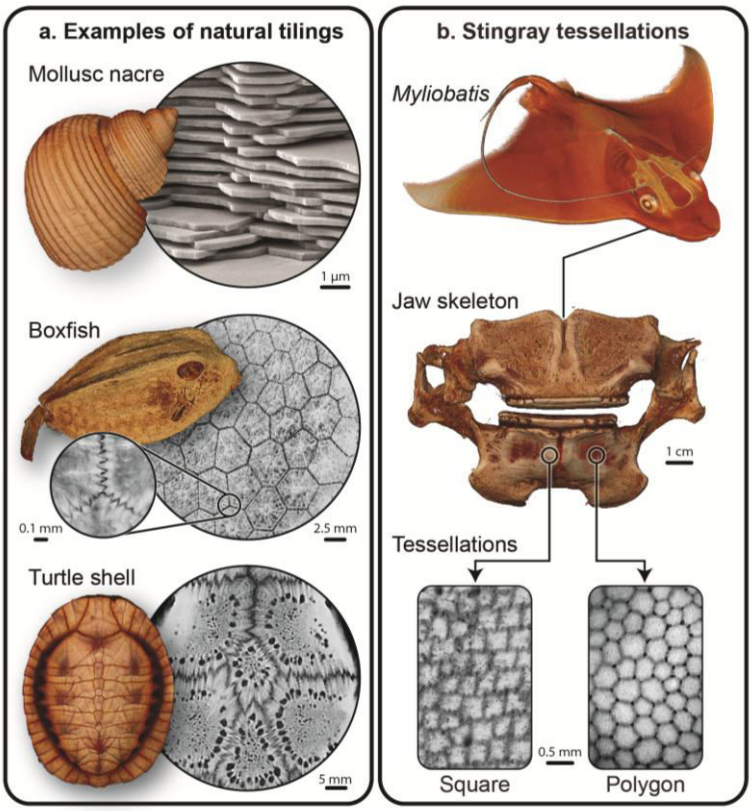

Figure 1: a. Examples of natural tilings, none of which are true tessellations due to overlapping (mollusc nacre) or interdigitating (turtle shell, boxfish scute) morphologies. b. Polygonal and square tessellations found in stingray cartilage. Organism and tissue images are compiled from a variety of species: a. Turbo caniculatus (mollusc shell), Haliotis rufescens (nacre); Phrynops geoffroanus (turtle shell); Ostracion rhinorhynchos (boxfish and scute inset; MCZ4454), Lactoria cornuta (interdigitations). b. Myliobatis freminvillei (stingray; USNM204770), Myliobatis californica (jaws; MCZ886), Aetobatus narinari (square tessellation), Leucoraja erinacea (polygonal tessellation).

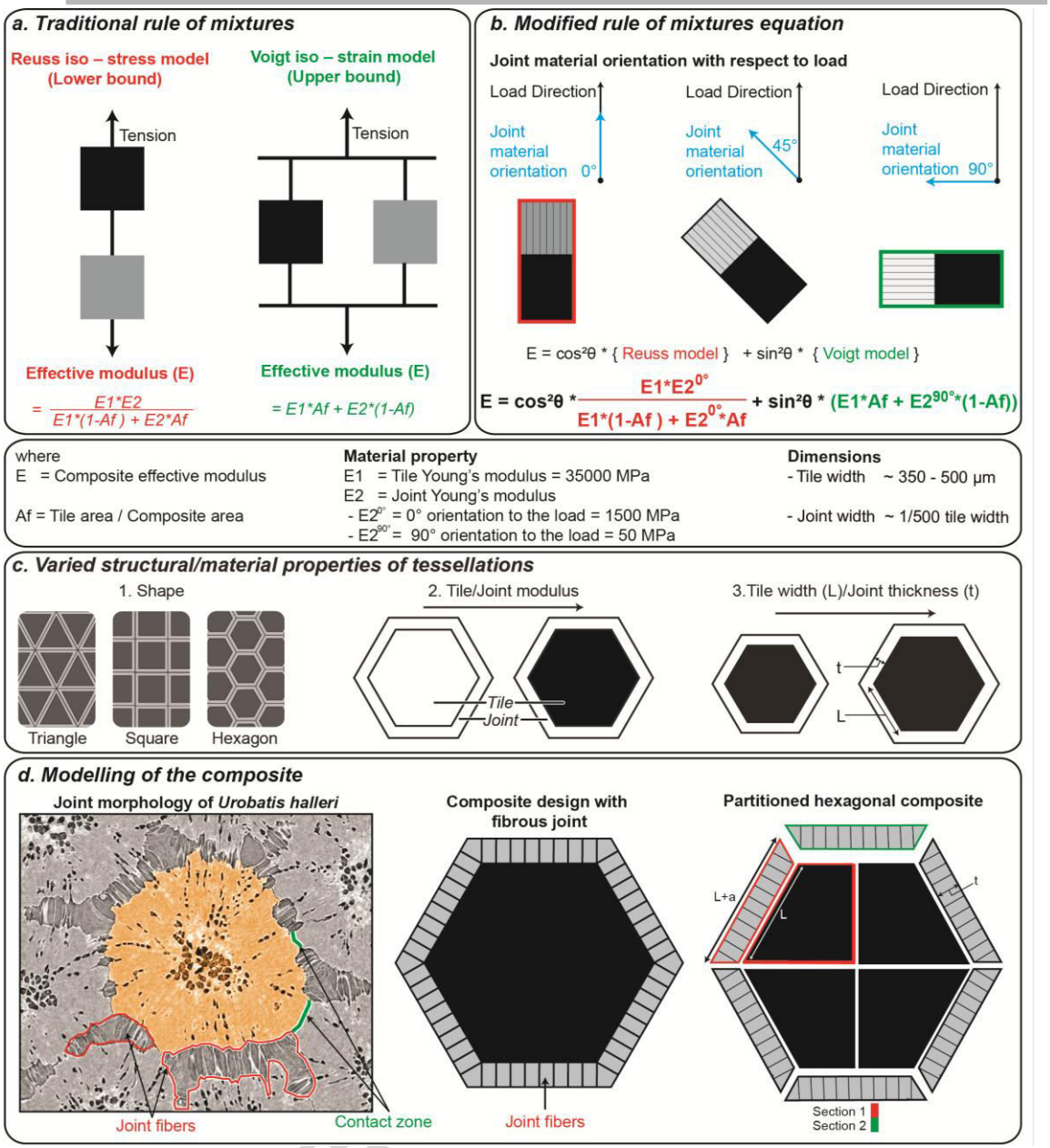

Figure 2: a. Rule of Mixtures: Reuss and Voigt models. b. Orientation of model with respect to direction of load and the effect on joint material Young's modulus and composite effective modulus (modified Rule of Mixtures). *c. Structural and material properties of tessellations varied in this study, including shape, tile/joint material, and tile area/joint width. d. Modelling of the composite with the inspiration derived from Urobatis halleri (see text for explanation); the partition of hexagonal tile composite. See the Appendix for full derivations for all three tile shapes.*

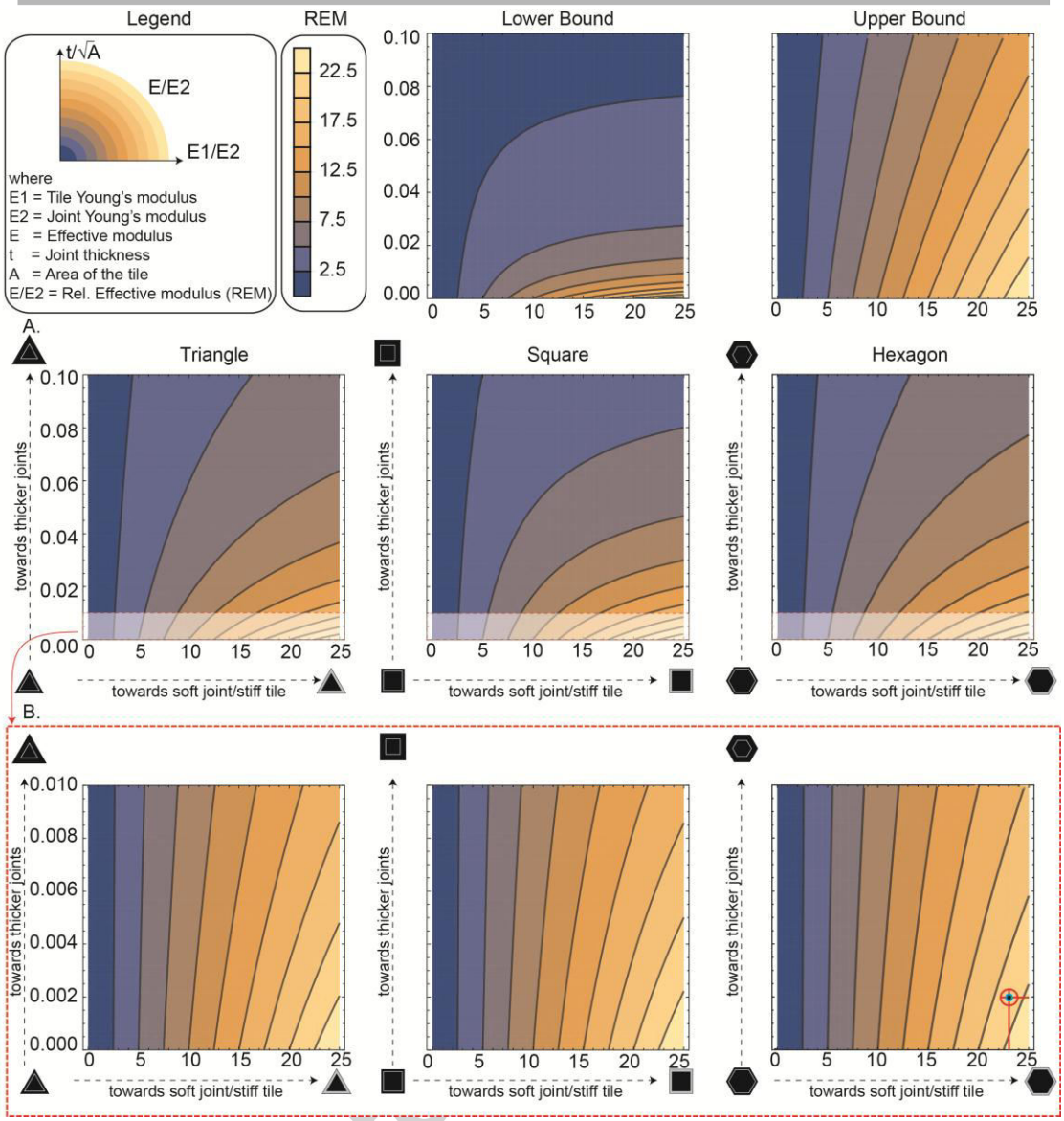

Figure 3: Relative Effective Modulus (REM) for all tile shapes, as a function of E1/E2 (x-axis) and t/√A (y-axis). The legend for terminology and scale for all graphs is shown in the upper left corner; with increasing x-axis values, tiles become stiffer relative to joints, with increasing y-axis values, joints are thicker relative to tile size. The lower and upper bounds for the square tile are shown in the upper right corner; upper/lower bound graphs for triangle and hexagon tiles were similar. A. Contour plots for all shapes (y-axis scale: 0.0-0.1). B. A zoomed in view of the contour plot from Figure 3A, to focus on more biologically relevant y-axis values (0.0 - 0.01). The biologically relevant x- and y-axis values —calculated from the structural and material properties of round stingray (U. halleri) tesserae— are marked by a red marker. Note that whereas hexagon result in the stiffest composite behavior overall (i.e. the REM values are highest for any given x-value), all tile shapes have similar contour patterns for the biologically-relevant range in B indicating little effect of unit cell shape on REM for thin joints (low y-axis values).

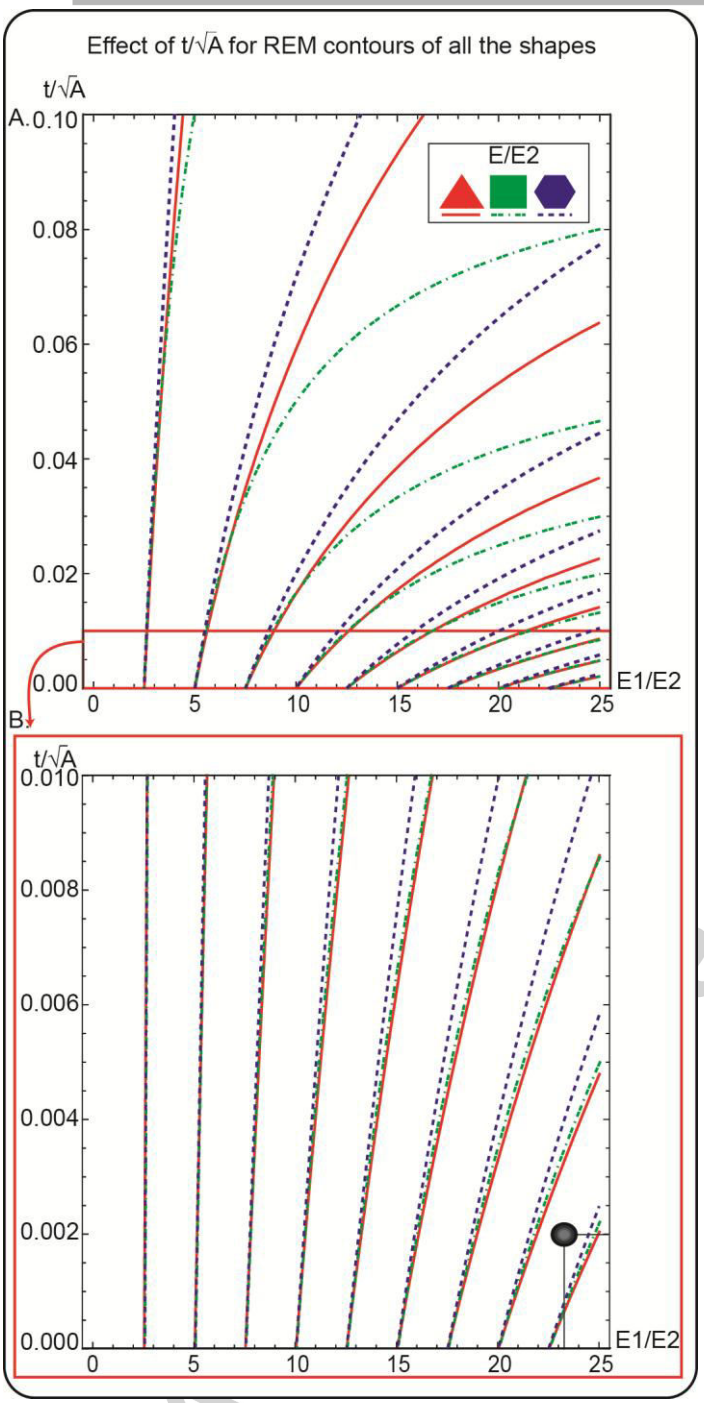

Figure 4: Comparison of the contour plots of all tile shapes from Figure 3. Contour lines originating from the same x-axis value (a contour line trio) correspond to the same z-axis value range (e.g. all lines in the first trio on the far left of 4A indicate REM = 2.5). The spread of contour line in a trio reflects the dissimilarity of the topography of the contour plots of the three tile shapes: in particular for the upper right portion of A, where joints are very thick and tiles are far stiffer than joints, the REM for hexagon is considerably higher than that of square. The narrower spread of contour lines in trios in biologically relevant range (B) indicates that unit cells exhibit more similar mechanical behavior at small y-axis values (e.g. narrow joints). A. Contour lines for all shapes (y-axis scale: 0.0-0.1); compare with Figure 3A. B. A zoomed in view of the contour plot lines from Figure 4A, to focus on more biologically relevant y-axis values (0.0 - 0.01); compare with Figure 3B. Values for the

structural and material properties of round stingray (U. halleri) tesserae are marked by a black marker.

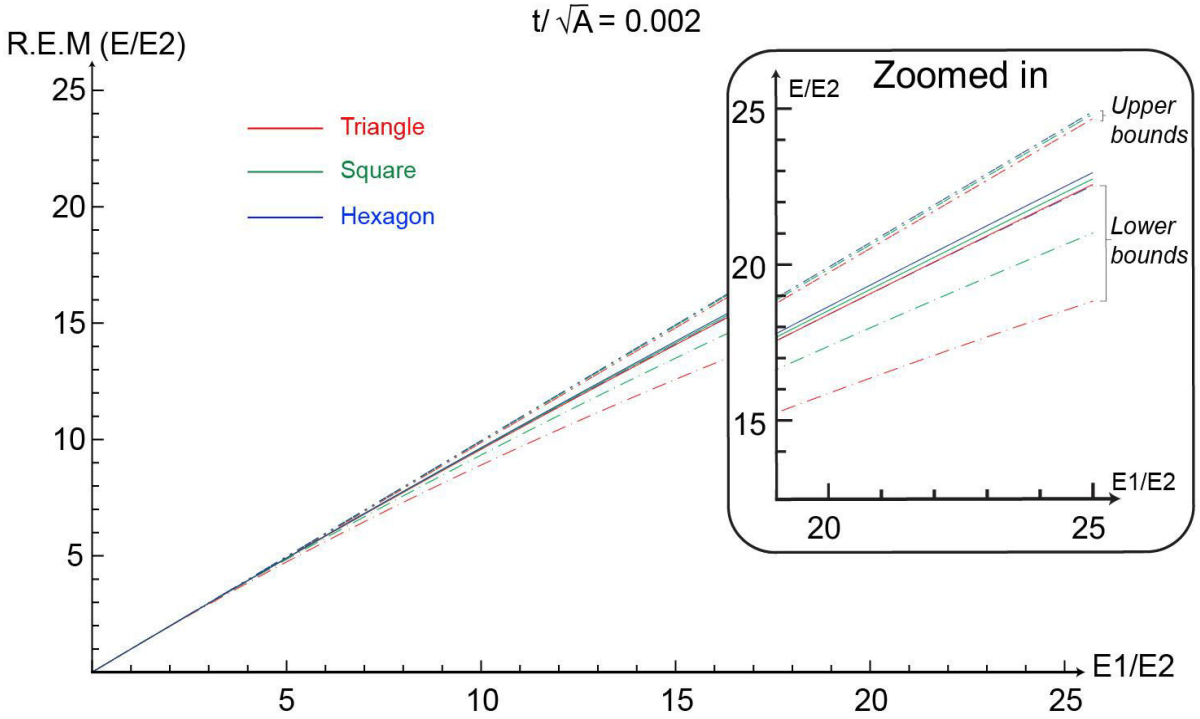

Figure 5: Two-dimensional graphical representation of REM for all tile shapes when t/sqrt(A)= 0.002 (biologically relevant value, derived from U. halleri tessellated cartilage), showing the relationship between tile and composite modulus. The zoomed in pane shows the high correspondence of the three unit cells' lines, indicating similar mechanical behavior at small y-axis values (e.g. narrow joints). All shapes fall within their respective upper and lower bounds; note that the upper bound lines are nearly overlapping and the lower bound for hexagon is hidden beneath the REM line for the triangle array. The region above the upper bound lines represents an unrealistic scenario where the composite is stiffer than its stiffest constituent (E>E1).

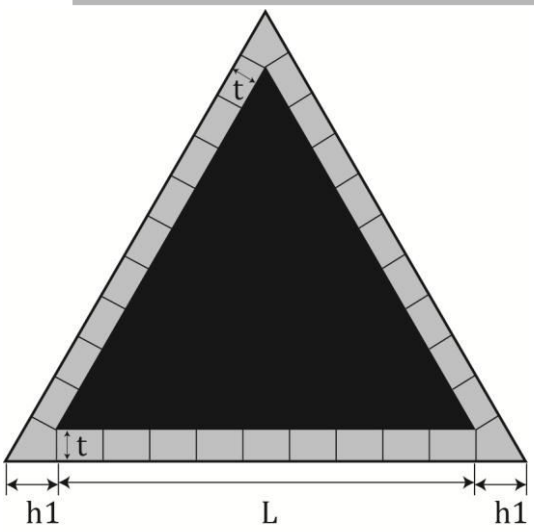

Figure A.1: Dimensions of triangle composite.

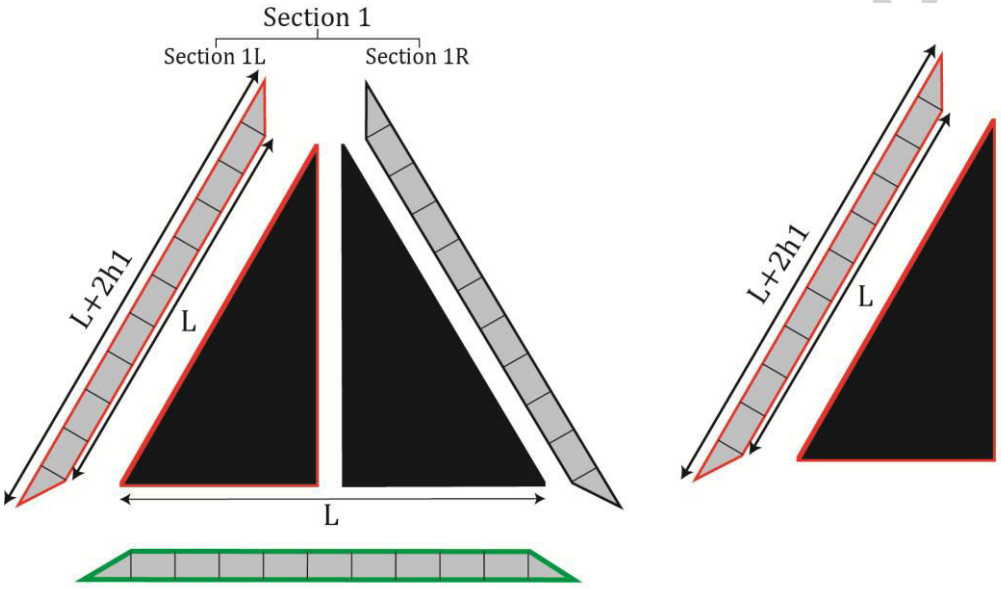

Figure A.2: Partitions in triangle composite.

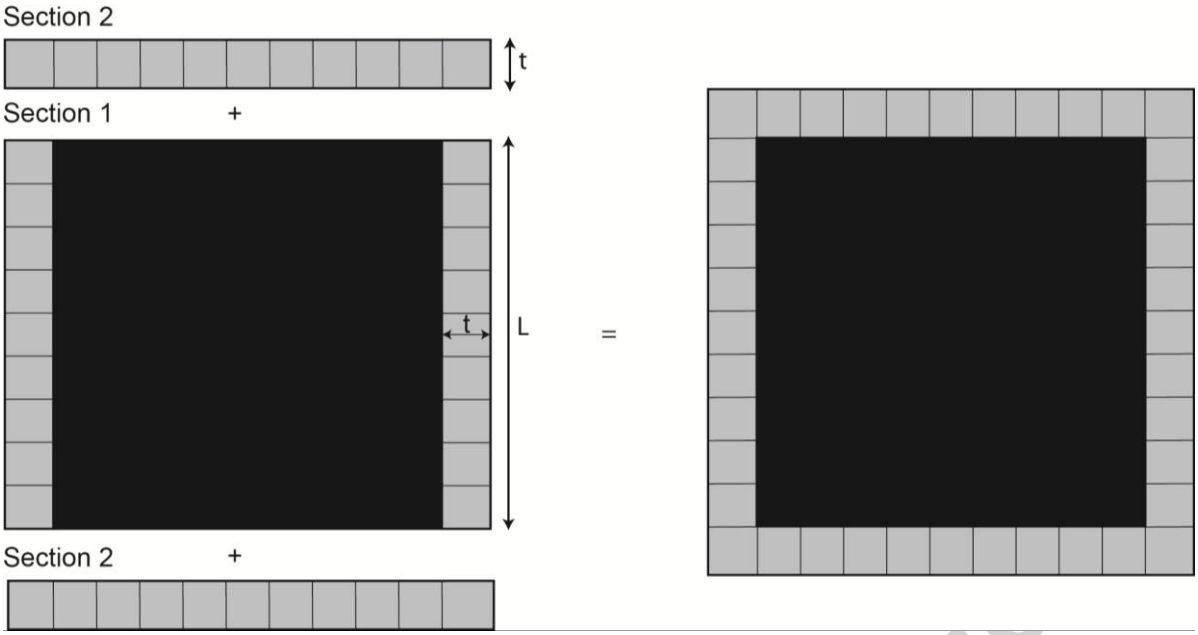

Figure A.3: Dimensions and partitions of square composite.

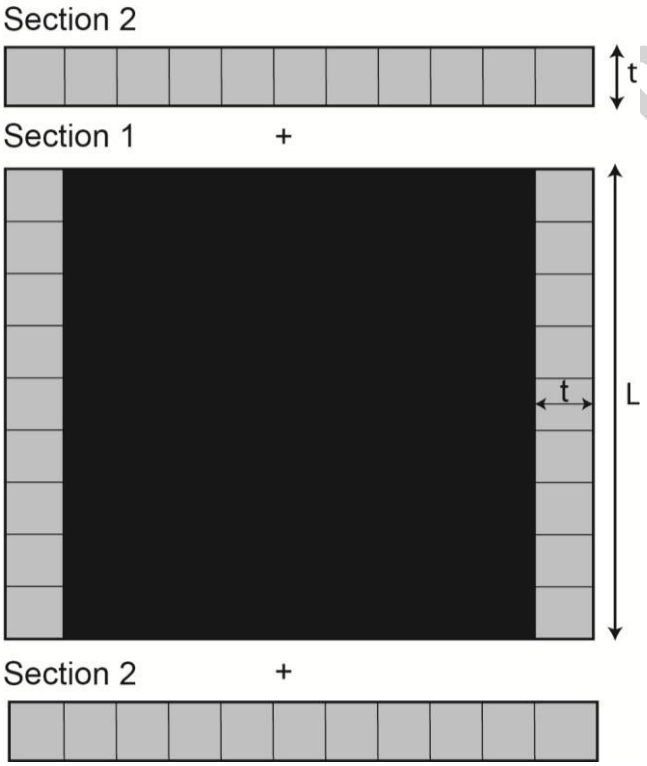

Figure A.4: Dimensions and partitions of Section 2 in square composite.

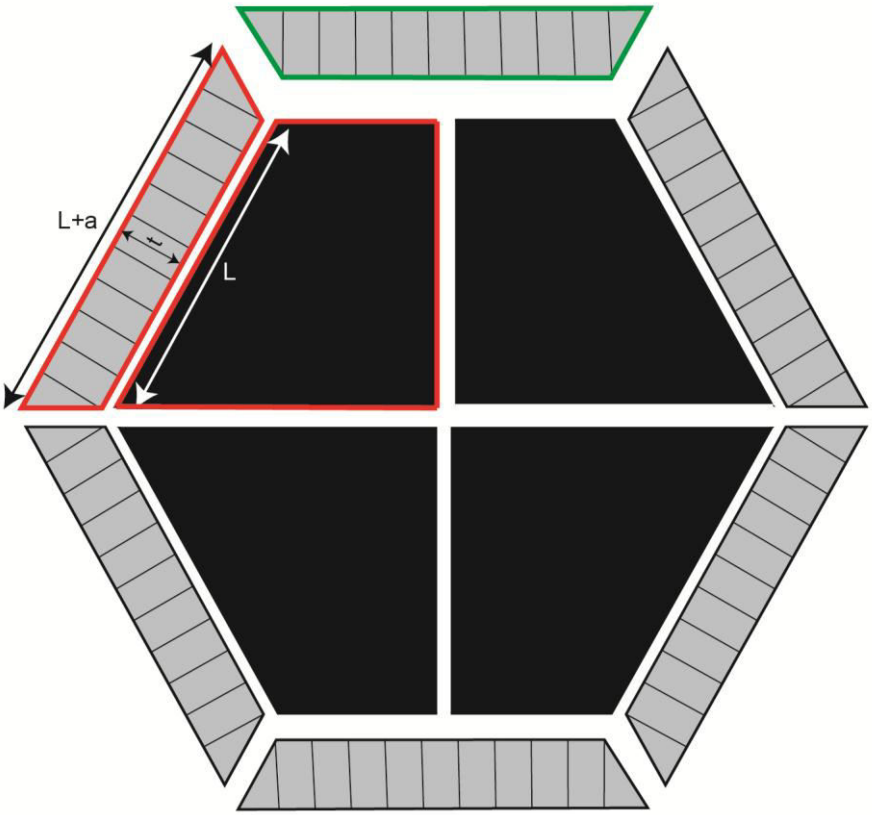

Figure A.5: Dimensions of hexagonal composite.

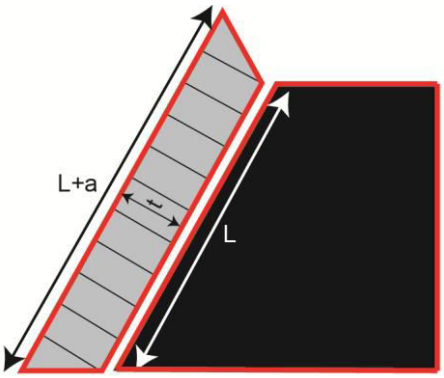

Figure A.6: Dimensions of partitions of hexagonal composite.

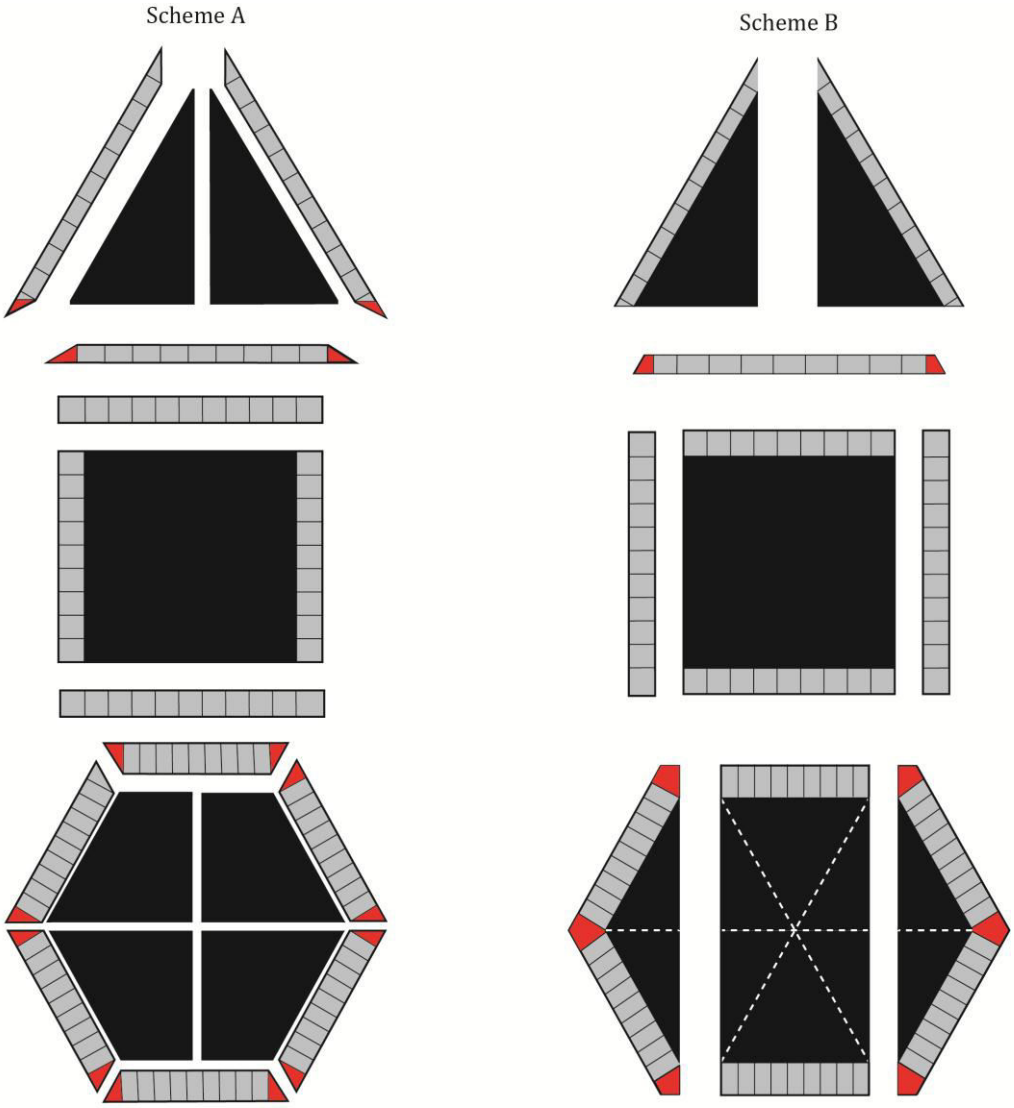

Figure A.7: Partitioning schemes. Regions colored in red indicate corner elements that are assigned different properties as a function of the different partitioning schemes.

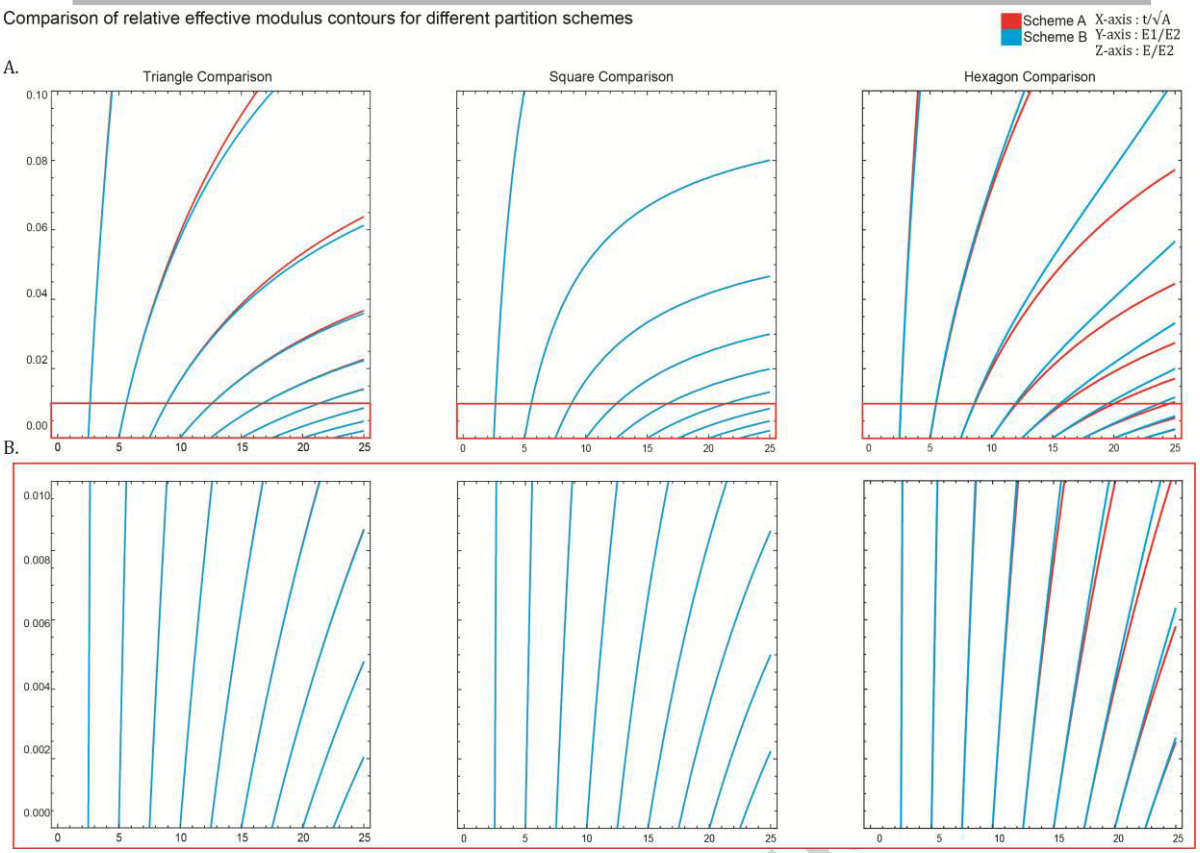

Figure A.8: Comparison of REM contour lines scheme. The two partition schemes shown in Fig. A.7, and on comparison with their REM lines they correlate with each other in the biological region of interest.

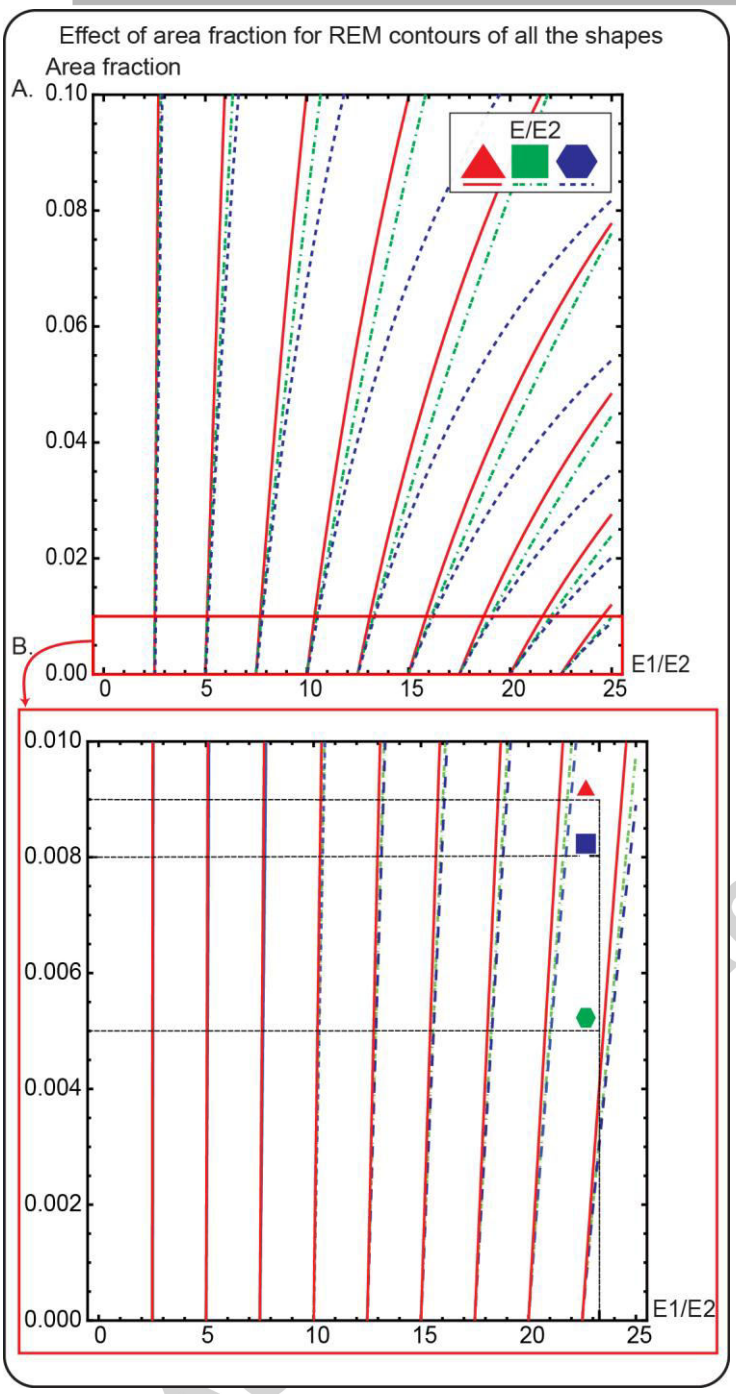

Figure A.9: Comparison of relative effective modulus for all shapes with respect to area fraction reflecting the REM values for all shapes lie in same contour region.

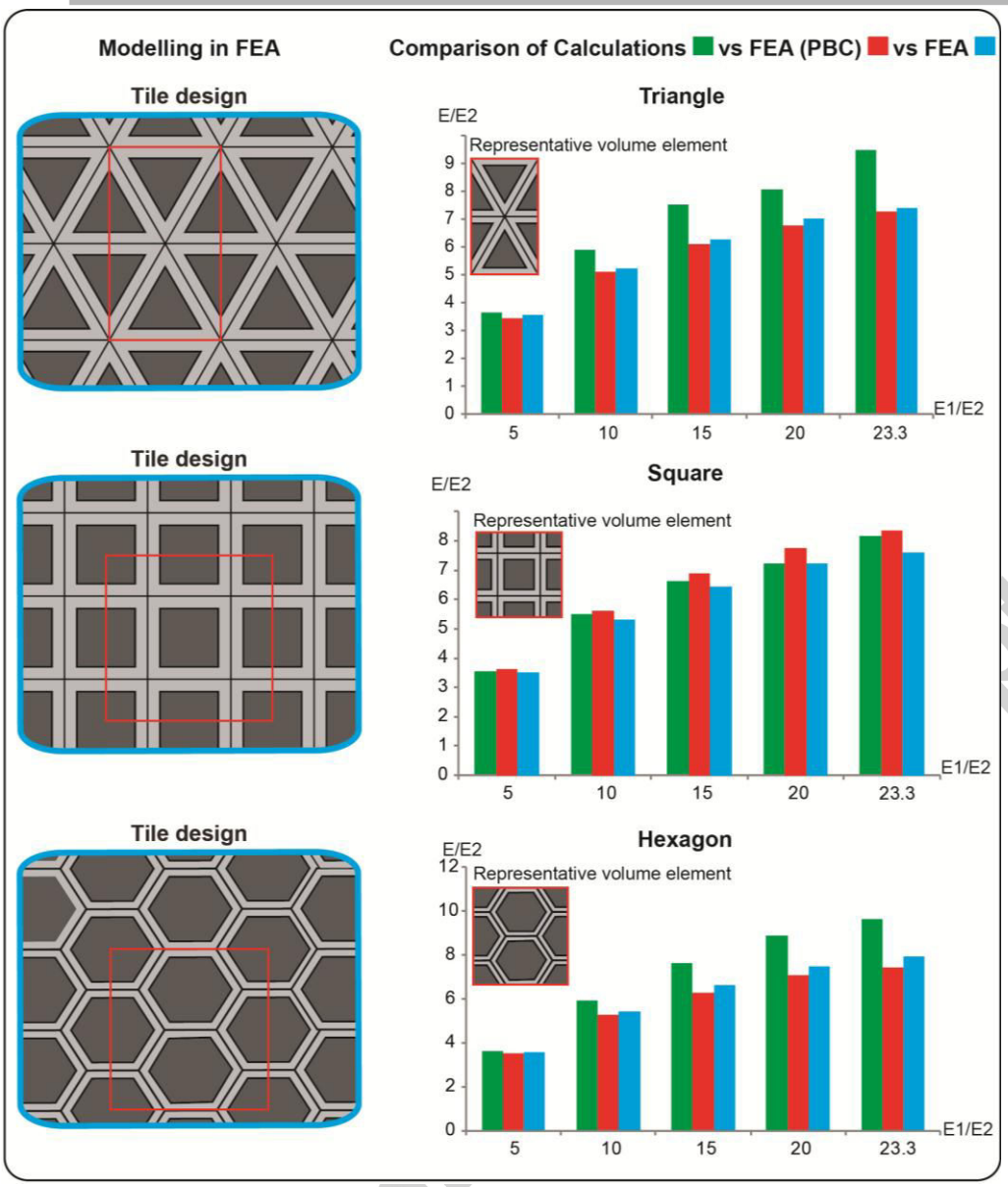

Figure A.10: Comparison of relative effective modulus (E/E2) between analytical calculations, FEA (periodic boundary conditions) and FEA (tiled array) with E1/E2 on x-axis and E/E2 on y-axis.